The Astrophysical Journal, 973:106 (13pp), 2024 October 1 https://doi.org/10.3847/1538-4357/ad64d6

A Portrait of the Rotation of Ultra-cool Dwarfs Revealed by TESS

D. O. Fontinele[1], P. D. S. de Lima[1,2], Y. S. Messias[1,3], R. L. Gomes[1,3], C. E. Ferreira Lopes[4,5], B. L. Canto Martins[1,6], I. C. Leão[1], J. M. De Araújo[1], E. Janot Pacheco[7,8], and J. R. De Medeiros[1]
[1] Departamento de Física Teórica e Experimental, Universidade Federal do Rio Grande do Norte, Campus Universitário, Natal, RN, 59072-970, Brazil; renan@fisica.ufrn.br
[2] School of Physics, Trinity College Dublin, Dublin 2, Ireland
[3] Département de Physique, IREX, Université de Montréal, Montréal, QC, H3C 3J7, Canada
[4] Instituto de Astronomía y Ciencias Planetarias, Universidad de Atacama, Copayapu 485, Copiapó, Chile
[5] Millennium Institute of Astrophysics, Nuncio Monseñor Sotero Sanz 100, Of. 104, 7500000 Providencia, Santiago, Chile
[6] INAF—Osservatorio Astrofisico di Arcetri, Largo Enrico Fermi 5, 50125 Firenze, Italy
[7] Instituto de Astronomia, Geofísica e Ciências Atmosféricas, Universidade de São Paulo, 05509-090, São Paulo, SP, Brazil
[8] Observatoire de la Côte d'Azur, Laboratoire Lagrange, Bâtiment Fizeau, Parc Valrose, 06108 Nice, France
Received 2023 December 16; revised 2024 May 26; accepted 2024 May 27; published 2024 September 24

Abstract

This study presents the results of a search for rotation signatures in 250 Gaia Data Release 3 ultra-cool dwarfs (UCDs) with TESS light curves (LCs). We identified 71 targets with unambiguous periodicities, of which 61 present rotation signatures and a single-source behavior, with periods between 0.133 and 5.81 days. Five UCDs show double-dip features, namely variations with two periods, one approximately double or half the other. The remaining 10 UCDs with unambiguous variability present a likely nonsingle behavior. We also found 20 UCDs showing complex behavior in their LCs, with noticeable fluctuations and irregular structure, with a few exhibiting apparent changes in their temporal structure. The remaining 159 targets show noisy LCs corresponding to low-amplitude signals, whose temporal variation cannot be easily identified. The distribution of the UCDs with rotation signature in a color–magnitude diagram points to a lack of rotating objects within about $11.5 < M_G < 12.5$ and G–$G_{\rm RP} < 1.5$, separating them into two regimes, one mainly composed of less massive late-M stars with $P_{\rm rot} \geqslant 1.0$ day, and another mainly composed of more massive early-M stars with $P_{\rm rot} < 1.0$ day. It is important to emphasize that by separating stars into age intervals, one observes that UCDs with $P_{\rm rot} \geqslant 1.0$ day tend to be located in regions of younger objects, and, in contrast, those with $P_{\rm rot} < 1.0$ day are mainly concentrated in regions of older objects. Whether this trend of stars contrasting the sample separation is physical or produced by observational biases is a question to be verified in future studies.

Unified Astronomy Thesaurus concepts: Low mass stars (2050); Stellar rotation (1629); Brown dwarfs (185); Stellar photometry (1620); Space observatories (1543); Stellar astronomy (1583)

Materials only available in the online version of record: figure sets, machine-readable tables

1. Introduction

Ultra-cool dwarfs (UCDs) are defined as objects with spectral types M7 or later, including L, T, and Y types, of stellar and substellar nature. These objects are characterized by intense and broad potassium lines in the optical, and water, methane, and ammonia absorption bands in the near-IR (e.g., Kirkpatrick et al. 1999; Burgasser et al. 2002; Burningham et al. 2008). Among their most interesting characteristics is the formation of atmospheric cloud-like structures, composed of iron and silicates for L dwarfs, chlorides and sulfides for T and early-type Y dwarfs, and water clouds in the coolest Y dwarfs (e.g., Saumon et al. 2000; Zahnle & Marley 2014; Suárez & Metchev 2023). Another fundamental characteristic of the UCDs concerns their well-established variability, characterized by brightness changes caused by large-scale atmospheric structures, such as spots or longitudinal bands, which can provide fundamental information on the physical processes operating at their atmospheres (e.g., Artigau et al. 2009; Buenzli et al. 2014; Radigan et al. 2014; Metchev et al. 2015).

To date, the literature has reported a growing list of studies on the photometric variability of UCDs, based on observations from ground-based telescopes (e.g., Tinney & Tolley 1999; Koen et al. 2005; Harding et al. 2013; Radigan et al. 2014; Miles-Páez et al. 2017), and from space (e.g., Buenzli et al. 2014; Metchev et al. 2015; Cushing et al. 2016; Tannock et al. 2021; Vos et al. 2022; Miles-Páez et al. 2023; Petrucci et al. 2024). These studies revealed essential characteristics on the behavior of the periodicities, including a clustering of shortest rotation periods near 1 hr (Tannock et al. 2021) and a lower envelope of rotation periods that runs from 2 hr at spectral type M8 down to 1 hr at spectral type T (Miles-Páez et al. 2023). Nevertheless, the astrophysical root cause for the variability in UCDs still needs to be better understood. On the stellar side of the hydrogen-fusing limit, starspots are the usual explanation for the observed variability (e.g., Rockenfeller et al. 2006; Irwin et al. 2011; Donati et al. 2023). For the UCDs, the variability can have multiple origins, such as magnetic processes (e.g., Hooten & Hall 1990), condensated particles that form atmospheric cloud-like structures (Tsuji et al. 1996), or even brightness changes due to an atmosphere out of chemical equilibrium (Tremblin et al. 2015). Pineda et al. (2017) pointed to evidence for a complex interplay between the starspots driving the variability of UCDs and robust large-scale magnetospheric current systems.

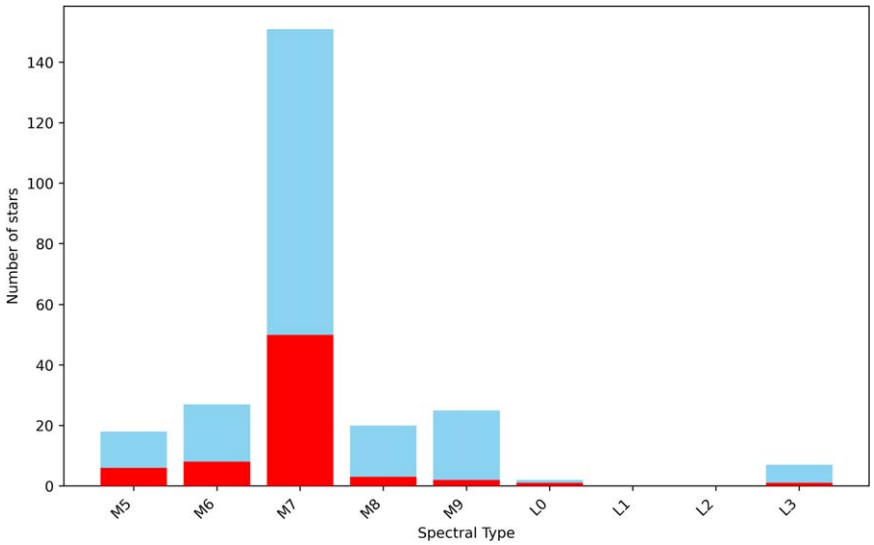

Figure 1. Distribution of spectral types for the present working sample of 250 UCs with bona fide TESS LCs. Red color stands for UCDs with unambiguous rotation and blue represents the entire UCD sample.

The NASA TESS space mission (Ricker et al. 2015), launched in 2018, is producing differential photometric light curves (LCs) for hundreds of thousands of stars. Primarily dedicated to the search for terrestrial planets transiting nearby bright stars, the large number of observed targets combined with the high quality of the acquired data is opening new horizons for the study of a variety of astrophysical phenomena, including stellar rotation and activity (e.g., Canto Martins et al. 2020; Doyle et al. 2020; Barraza et al. 2022). Thanks to its high-quality photometry data and continuous monitoring, TESS could also represent an optimal laboratory for the search for rotation periods in UCDs.

Aiming to enlarge the current sample of UCDs with measured rotation periods, this study is dedicated to the search for rotation signatures in sources identified as UCDs in the Gaia Data Release 3 (DR3; Sarro et al. 2023), observed by the TESS mission. This paper is part of a collaborative effort to determine rotation periods for different families of stars located throughout the Hertzsprung–Russell diagram, with LCs collected by the referred space mission. The paper is organized as follows. Section 2 presents the stellar sample and observational data set used in this study and the procedure used to analyze the LCs. Section 3 provides the main results. A summary is presented in Section 4.

2. The Ultra-cool Dwarf Sample and Observational Data Analysis

The TESS primary mission plan is to survey almost the entire sky by monitoring 26 segments (or sectors) of $90^\circ \times 24^\circ$, each one with a duration of 27 days at a time, with four on-board 10.5 cm telescopes in a red (600–1000 nm) bandpass. A given sector is, therefore, revisited about every 2 yr. However, overlaps between sectors can increase the coverage, and targets in the continuous viewing zone (CVZ) are observed with almost unbroken coverage for 1 yr. The mission provides photometric time series at different cadences, namely 2 and 30 minutes in Cycles 1 and 2, and 20 s, 2 minutes, and 10 minutes in Cycle 3, with a time baseline from 27 to 351 days, depending on sector overlaps. While 2 minutes cadence data, also known as target pixel (TP) files, are available for a subset of targets, all CCDs, called full-frame images (FFIs), are read out every 30 minutes (10 minutes in the extended mission). Ten subsets of TESS targets were observed for multiple sectors, with approximately 1%–2% of targets located in the CVZ during the primary mission (Barclay et al. 2018). Such an aspect makes these targets invaluable for extracting rotation periods and analyzing the persistence of stellar cycles (Ferreira Lopes et al. 2015).

For this study, searching for rotation signatures in UCDs and determining their periods, we have used the sample of 7630 Gaia DR3 UCDs, given by Sarro et al. (2023), as a starting point. For the definition of this sample, those authors used the Gaia DR3 set of UCD candidates and complemented the Gaia spectrophotometry with additional photometry to characterize the candidates' global properties. This procedure includes the determination of the distances and their locus in the Gaia color–absolute magnitude diagram (CAMD). More specifically, they present the typical (median) spectra in the red photometer (RP) band of Gaia, organized by spectral type, and compare them to UCD standards, ground-based high-resolution spectra, and CAMDs, including Gaia and external photometry. Then, that sample was compared with the TESS Input Catalog (TIC), from which 7360 objects were identified out of the total sample of 7630. Of this latter list, we found 250 targets with TESS 2 minutes cadence LCs available on 2023 October 30. On this date, the TESS data basis also reported observations of 674 targets in a 30 minutes cadence, 124 in a 10 minutes cadence, and one target in a 20 segment cadence; all these additional data are not suitable for our purpose.

The 2 minutes cadence data were downloaded from the FFI-TP-LC-DV Bulk Downloads page of the Mikulski Archive for Space Telescopes using the cURL scripts available for retrieving Pre-search Data Conditioned Simple Aperture Photometry (PDCSAP) reduced LCs.[9] Jenkins et al. (2016) describe the TESS Science Processing Operations Center (SPOC) pipeline that produces the 2 minutes cadence LCs. The distribution of the spectral types for the list of 250 UCDs with TESS LCs is displayed in Figure 1, which ranges from M5 to L3. The referred spectral types were computed following the

[9] https://archive.stsci.edu/tess/bulk_downloads.html

calibration by Pecaut & Mamajek (2013). These targets are located in the following star-forming regions, open clusters, or moving groups, as listed in Table A1 of the Appendix: Taurus (TAU), Carina-Near (CARN), the Tucana-Horologium Association (THA), the ϵ Chamaeleontis Association (EPSC), the AB Doradus moving group (ABDMG), the β Pic moving group (BPMG), Upper Centaurus Lupus (UCL), Hyades (HYA), the TW Hya Association (TWA), the Lower Centaurus Crux (LCC), the Pleiades cluster (PLE), Columba (COL), Argus (ARG), Coma Berenices (CBER), and the Carina Association (Car). The determination of membership to the referred star clusters and moving groups were derived by Sarro et al. (2023), using the BANYAN Σ software tool (Gagné et al. 2018). Those authors have used the Gaia DR3 UCD candidates, namely their celestial positions and proper motions and parallaxes, as input to BANYAN Σ.

When required, additional processing on these LCs was performed manually to avoid possible distortions in the variability signatures. Such processing explicitly involved the removal of outliers and correction of instrumental trends, following the prescription by De Medeiros et al. (2013), Paz-Chinchón et al. (2015), and Canto Martins et al. (2020). In short, flux measurements exceeding 3 times the standard deviation of the LC compared to the average neighbor data were considered outliers and then removed from the time series. The correction of instrumental trends consisted of detrending the LC of each sector from a polynomial fit of third order. In the analysis of the post-processed LCs for the 250 UCDs with TESS observations, we have used the same procedure as applied by Canto Martins et al. (2020), which is based on a manifold interactive platform built in IDL.[10] Readers are referred to Canto Martins et al. (2020) and Barraza et al. (2022) for a complete description of the referred manifold package. In short, our analysis consisted of computing fast Fourier transform (FFTs; e.g., Zhan et al. 2019), Lomb–Scargle periodograms (e.g., Scargle 1982; Horne & Baliunas 1986; Press & Rybicki 1989), as well as wavelet maps and global spectra (Grossmann & Morlet 1984) of each LC. Based on the known range of the rotation periods of UCDs (e.g., Bailer-Jones 2004; Tannock et al. 2021), we searched for the main periodicities, namely peaks, computed from those methods. The errors on the corresponding peak periods were estimated using Equation (2) of Lamm et al. (2004). The Lomb–Scargle method was also used to consider the false-alarm probability (FAP) of the periodicities, based on Equation (22) of Horne & Baliunas (1986), given by $F = 1 - \{1 - \exp[-(N_0/2)(1 + xi^{-1}) - 1]\}^{N_i}$. The formula gives the periodogram power threshold, F, corresponding to a given FAP, ξ, where N_0 is the number of observations of a LC, ξ is the FAP, and N_i is the number of independent frequencies, namely $N_i = -6.362 + 1.193N_0 + 0.00098N_0^2$, according to Equation (13) of Horne & Baliunas (1986). In the present work, only peaks with a FAP less than 1%, corresponding to significance levels greater than 99%, were taken into consideration. Additionally, wavelet maps were used to examine the persistence of the main signals within the time span of TESS observations of a given target in different sectors, and phase diagrams of the possible periodicities were computed to inspect the global morphology of each signal.

After obtaining the FFTs, Lomb–Scargle periodograms, wavelet analyses, and phase diagrams results, we visually inspected each LC to identify the present modulation features, adopting the procedure applied by Canto Martins et al. (2020).

Specifically, we separated the targets into three groups: (i) those with a typical rotational modulation in the LC, namely a signature characterized by semi-regular flux variability that used to be multi-sinusoidal; (ii) those with an ambiguous, dubious, or complex variability profile, namely those targets with LCs displaying an asymmetric shape in the flux variation; and (iii) targets with noisy LCs. From the sample of 250 UCDs with bona fide TESS LCs, listed in Table A1 of the Appendix, we have identified 54 UCDs presenting unambiguous variability, with variability amplitudes ranging from 0.6% to 40.9%, for which we have computed the associated periods. This list of 54 UCDs is presented in Table 1, which also contains the referred periods. Figure 2 displays three examples of LCs with typical rotation signatures identified in our sample of UCDs, with the corresponding phase-folded LCs, FFTs, Lomb–Scargle periodograms, and wavelet maps. Figures following the same design as Figure 2 for all the UCDs with unambiguous variability are provided in the online figure sets given in Figure B1. Among the UCDs with evident variability, we identified 20 targets presenting a complex temporal structure in their LCs. The referred LCs are also provided in an online figure set given in Figure B1.

2.1. A Search for Periodicities in Gaia DR3 UCDs with Supposedly Noisy LCs

Our manifold analysis has initially identified 176 Gaia DR3 UCDs with LCs presenting supposedly noisy signatures, an aspect assumed particularly for LCs with a low-amplitude signal. Indeed, as underlined by different studies (e.g., Gilliland et al. 2011; Canto Martins et al. 2020), such noisy behavior is a complex combination of different factors, including, for example, instrumental noise contributions and data-reduction processes. Some UCDs classified as having noisy LCs may have been classified this way because of data-reduction issues.

Considering that different studies point to a clustering of shortest rotation periods of UCDs near 1–2 hr (e.g., Tannock et al. 2021; Miles-Páez et al. 2023), we revisited the sample of 176 Gaia DR3 targets with LCs previously classified as noisy in the search for short periods, specifically for periods shorter than 1 day. First, we reanalyzed each LC using the wavelet method to search for persistent temporal structures on timescales shorter than 1 day, all along the considered LC time span. Such a procedure revealed 17 targets with potential low-amplitude variability ranging from 0.22% to 21%, a signature also clearly visible in the related phase-folded LCs. For these targets, it was possible to compute wavelet (WT) and Lomb–Scargle (LS) periods, listed in Table 2, with the respective variability amplitude. Table 2 lists sectors where it was possible to extract the period variability and sectors with negligible or absent modulation. To reinforce the presence of variability with potential physical meaning, not reflecting instrumental systematics, we have analyzed the LCs of these 17 UCDs using the so-called W transform (Wang 2021, 2022), which computes a time–frequency as the wavelet transform, but with a significant difference: The W transform uses a nonstationary window function to concentrate the spectral energy in the region of a dominant frequency and to remove the singularity problem related to the zero frequency in the time–frequency spectrum. Indeed, whereas the standard wavelet transform shifts the energy of a signal toward a higher frequency, the W transform centralizes the referred energy around

[10] https://www.l3harrisgeospatial.com/Software-Technology/IDL

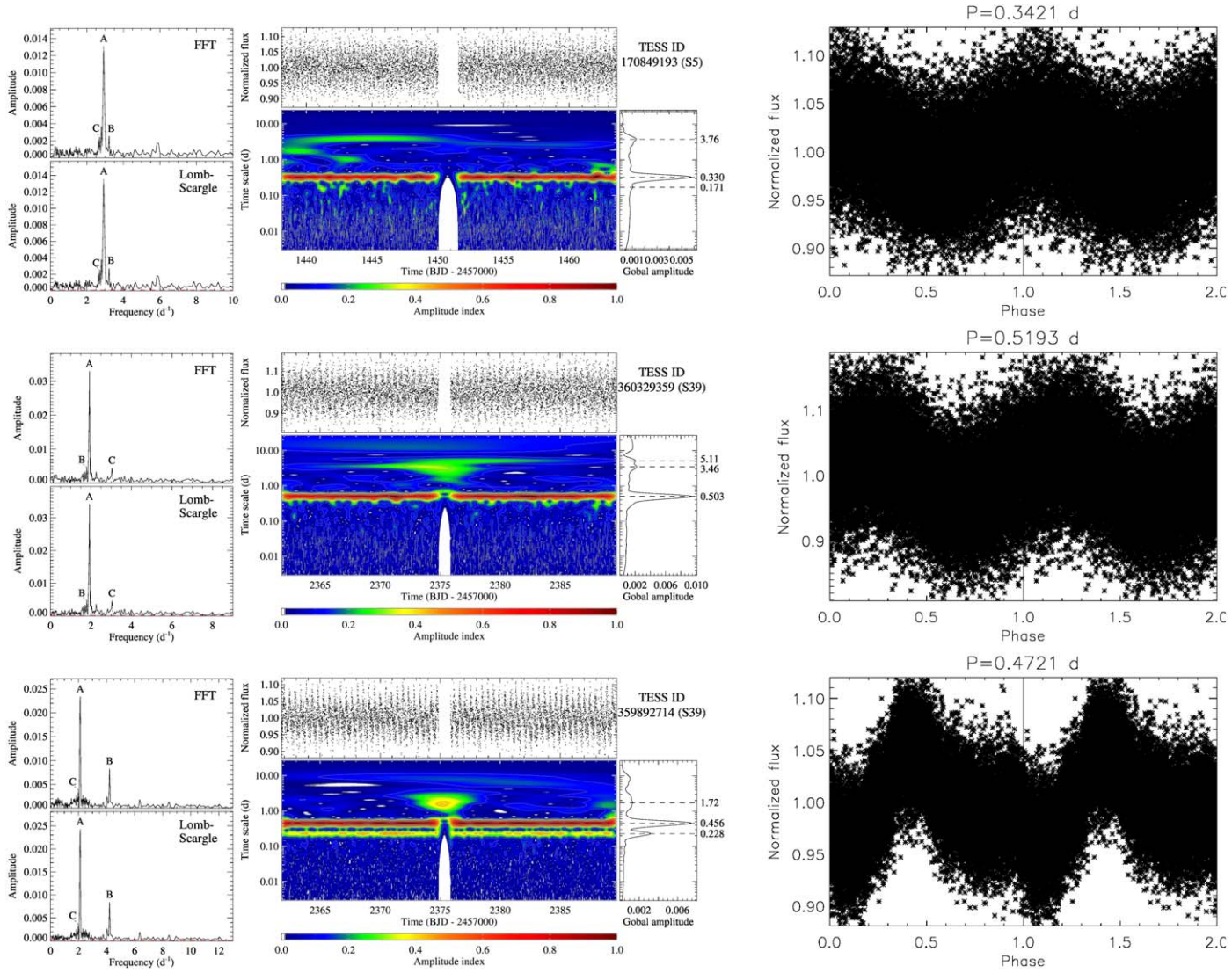

Figure 2. Examples of diagnostic plots displaying FFT and Lomb–Scargle periodograms, LCs, phase-folded LCs, and wavelet maps for three Gaia DR3 UCDs with typical TESS rotation signatures. A rersistent rotation period variability of 0.329, 0.519, and 0.472 day, respectively, for TIC 170849193 (top panels), TIC 360329359 (middle panels), and TIC 359892714 (bottom panels) is observed in their wavelet maps and confirmed by the FFT and Lomb–Scargle peaks, labeled "A." Figures for the entire sample, following the same design, are provided in the figure set given in Appendix B.

Table 1
Gaia DR3 UCDs with TESS Unambiguous Periodicities

TIC ID	Gaia ID	P_{rot} (days)	eP_{rot} (days)	t_{SPAN} (days)	N_{Cycle}	Sectors	CROWD	RUWE	Age (Myr)
5630425	3493736924979792768	1.499	0.018	21.000	14.000	10	0.494	1.104	24(a)
17308621	48193316928788352	1.332	0.020	43.981	33.019	43, 44	0.589	1.357	2(b)
17518894	3314586142482134144	2.065	0.049	43.916	21.267	43, 44	0.988	1.491	2(b)
20305594	1388684770725399296	0.563	0.001	73.210	260.534	23, 24, 50, 51	0.994	1.183	149(a)
45193132	5314960632252986880	2.486	0.025	123.355	49.620	8–10, 35–37	0.093	1.01	149(a)
49178529	5401822669314874240	0.967	0.022	21.503	22.237	36	0.436	1.085	10(a)
56002511	3185321611286286976	0.377	0.003	23.785	63.089	5	0.956	2.317	149(a)
56624850	163178353176600448	3.155	0.113	44.177	14.002	43, 44	0.782	1.551	149(a)
56658216	164802984685384320	2.606	0.077	44.140	16.938	43, 44	0.823	1.013	2(b)
56658273	164800235906367232	5.81	0.382	44.160	7.601	43, 44	0.894	0.888	2(b)
58229181	164513022853468160	2.11	0.050	44.140	20.919	43, 44	0.978	1.54	2(b)
58285779	164513400810646912	1.669	0.063	22.000	13.182	44	0.183	1.205	2(b)
58436495	150501362066641664	0.58	0.004	43.885	75.664	43, 44	0.270	0.979	2(b)
58538719	152516079683687680	2.447	0.068	44.046	18.000	43, 44	0.872	1.036	2(b)
58601455	152108882425024128	4.66	0.251	43.211	9.273	44	0.568	0.976	2(b)
58638214	152917298349085824	0.752	0.004	67.494	89.753	19, 43, 44	0.726	1.372	2(b)

Table 1
(Continued)

TIC ID	Gaia ID	P_{rot} (days)	eP_{rot} (days)	t_{SPAN} (days)	N_{Cycle}	Sectors	CROWD	RUWE	Age (Myr)
78772203	5424690587034982144	0.133	0.000	88.644	666.499	35, 36, 62, 63	0.173	1.08	40(c)
96680763	156915878541979008	0.302	0.001	44.205	146.423	43, 44	0.107	0.928	2(b)
101256057	216677698470254976	1.691	0.023	61.735	36.493	42, 43, 44	0.017	0.87	–
102076870	3459372646830687104	0.982	0.011	41.944	42.713	10, 37	0.412	1.068	10(a)
118520413	145238687096970496	1.498	0.026	43.212	28.846	43, 44	0.894	0.981	2(b)
125882806	148420639387738112	1.027	0.012	43.514	42.342	43, 44	0.980	0.944	2(b)
125977598	147441558642852736	4.418	0.223	43.794	9.913	43, 44	0.970	1.001	2(b)
150005829	148354733113981696	3.138	0.113	43.534	13.873	43, 44	0.895	1.285	2(b)
150058659	148400229703257856	3.438	0.136	43.566	12.672	43, 44	0.980	1.021	2(b)
150094175	157644373715415424	0.726	0.006	43.727	60.230	43, 44	0.674	1.109	2(b)
150122702	148196510814073728	3.782	0.164	43.681	11.550	43, 44	0.894	0.969	2(b)
167808464	5286310069347838080	0.279	0.000	145.412	583.983	7–13	0.223	0.99	45(a)
170849193	4877824564574114304	0.329	0.002	23.768	72.243	5	0.845	1.079	45(a)
232064183	6406967509044866560	0.718	0.006	41.292	57.510	27, 28	0.064	1.062	24(a)
268017136	151262876946558976	2.78	0.088	43.860	15.777	43, 44	0.767	0.995	2(b)
268018471	152466120624336896	2.037	0.047	43.914	21.558	43, 44	0.879	1.08	2(b)
268144659	152643240779301632	1.926	0.042	43.84	22.762	43, 44	0.287	1.033	2(b)
268148996	151327159721125888	1.389	0.022	43.38	31.231	43, 44	0.885	1.133	2(b)
268217504	149369139966814976	3.918	0.176	43.553	11.116	43, 44	0.966	1.095	2(b)
268218180	146366442430208640	2.382	0.065	43.528	18.274	43, 44	0.976	1.128	2(b)
268324394	146277553787186048	3.379	0.132	43.310	12.817	43, 44	0.555	1.049	2(b)
268324578	147799209159857280	2.248	0.058	43.346	19.282	43, 44	0.142	1.213	2(b)
268325250	151028990206478080	2.386	0.066	43.273	18.136	43, 44	0.723	1.5	2(b)
268397898	147801339463632000	1.004	0.012	43.282	43.110	43 ,44	0.987	1.353	2(b)
268399069	151130591952773632	1.866	0.040	43.456	23.288	43, 44	0.952	1.249	2(b)
298907057	3200303384927512960	0.484	0.005	23.879	49.337	5, 32	0.825	1.099	200(d)
359892714	5841324542416019712	0.458	0.000	97.523	427.733	11, 12, 38, 39	0.669	1.069	3.7 (e)
360329359	5919792529769594240	0.502	0.005	26.857	53.500	39	0.142	0.974	149(a)
367079252	2278720295036404736	2.769	0.029	132.993	48.029	17–19, 24–26	0.906	1.026	–
379097589	3724596914697213056	0.237	0.001	33.159	139.910	23, 50	0.606	1.146	200(d)
397287296	3314309890186259712	2.655	0.080	43.785	16.492	43, 44	0.826	1.125	2(b)
401838575	4954453580066220800	0.315	0.001	43.106	136.844	2, 3	0.978	1.178	45(a)
427770178	147614422487144960	1.479	0.025	43.355	29.314	43, 44	0.726	1.198	2(b)
440859813	6224387727748521344	2.04	0.047	44.361	21.746	11, 38	0.480	1.256	149(a)
454227159	5201185574182015744	2.042	0.020	51.000	25.07	38, 39	0.395	1.145	2(b)
454291779	5201129563515179520	3.23	0.075	70.000	21.672	11, 38, 39	0.848	1.024	–
456944264	3314299238667410176	2.22	0.056	43.834	19.745	43, 44	0.898	1.048	2(b)
902237947	3562157781229213312	0.241	0.001	21.439	88.884	36	0.210	3.117	200(d)
			Targets with Second Period						
20305594	1388684770725399296	0.281	0.002	73.210	130.035	23, 24, 50, 51	0.994	1.183	149(a)
58638214	152917298349085824	0.367	0.001	67.494	183.758	19, 43, 44	0.726	1.372	2(b)
96680763	156915878541979008	0.117	0.000	44.205	377.821	43, 44	0.107	0.928	2(b)
150094175	157644373715415424	0.966	0.011	43.727	45.266	43, 44	0.674	1.109	2(b)
359892714	5841324542416019712	0.228	0.001	97.523	212.932	11, 12, 38, 39	0.669	1.069	3.7(e)

Note. Ages are from (a) Bell et al. (2015), (b) Kenyon & Hartmann (1995), (c) Zuckerman et al. (2011), (d) Zuckerman et al. (2006), and (e) Murphy et al. (2013).
(This table is available in machine-readable form in the online article.)

the dominant frequency. The periodicity values computed from the W transform are also listed in Table 2, which reinforces those obtained from wavelet and Lomb–Scargle methods. Figures following the same design as Figure 2 for these 17 UCDs with likely rotation signatures and low-amplitude variability are provided in an online figure set in Appendix B2.

2.2. Cleaning the Sample of UCDs with Modulation

We have checked all the stars with unambiguous periodicities to verify if the variability signals obtained from their LCs were associated with the considered UCD. Indeed, given the TESS large plate scale of 21″ pixel^{-1}, analyses of signals obtained from the LCs of this mission should be undertaken with caution due to potential contamination by blended LCs, which can induce an interpretation of the observed variability to a wrong source (Mullally et al. 2022; Higgins & Bell 2023; Pedersen & Bell 2023). To assess the potential impact of contamination by nearby sources, we analyzed the crowding metric (CROWD) calculated by the SPOC pipeline (Caldwell et al. 2020), which indicates the fraction of the light in the TESS aperture that comes from the considered target given the positions and amplitudes of stars in the TIC. A CROWD value near 1.0 indicates a potentially isolated star, while lower values

Table 2
Gaia DR3 UCDs with Low Amplitude and TESS Unambiguous Periodicities

TIC ID	Gaia ID	P_{rot} (LS) (days)	Amplitude (%)	P_{rot} (WT) (days)	TESS Sectors with Modulation	Noisy TESS Sectors	CROWD	RUWE	Age (Myr)
26126812	68012529415816832	0.229	0.50	0.260	42, 43, 44		0.974	1.217	24(a)
50085560	2613754712222934656	0.427	0.80	0.444	42		0.978	0.958	149(a)
52256020	4691426694779173376	0.265	0.50	0.254	1, 2 , 27–29		0.971	1.292	45(a)
58432630	152284735566828032	0.642	0.85	0.690	43, 44		0.511	0.945	2(b)
201688405	6473160651658069120	0.692	0.39	0.731	27	13	0.850	0.983	149(a)
266012525	2556491429388743296	0.313	1.76	0.313	43		0.971	1.079	45(a)
275133493	3852362605385919616	0.438	0.73	0.446	8, 35	45	0.808	1.042	149(a)
281668854	4920330653311504256	0.116	0.56	0.118	2, 28, 29		0.877	9.984	45(a)
299007548	3230008650057256960	0.529	0.40	0.568	32	5	0.809	1.140	24(a)
302396416	1113083282052337792	0.458	0.42	0.464	19, 20, 26, 40, 47	60, 53	0.832	1.020	149(a)
342967337	5316349173696052736	0.705	2.62	0.697	8	9, 10	0.126	1.056	45(a)
356632694	1640572714166158976	0.240	0.27	0.260	14, 16, 21, 49	15, 22–24, 41, 48, 50	0.705	1.426	149 (a)
371080717	898275195732381440	0.714	0.35	0.714	20	60	0.311	1.057	40(c)
388682292	5514929155583865216	0.533	9.80	0.543	8		0.099	2.109	149(a)
405514195	6059992460039778560	0.237	2.90	0.240	11		0.160	1.047	15(d)
448590406	3478519134297202560	0.404	0.16	0.431	36	10	0.769	2.201	10(a)
959690391	5856405272135505024	0.221	21.69	0.223	38		0.005	1.144	149(a)

Note. Ages are from (a) Bell et al. (2015), (b) Kenyon & Hartmann (1995), (c) Zuckerman et al. (2011), and (d) Pecaut & Mamajek (2016).
(This table is available in machine-readable form in the online article.)

indicate a potential crowding from neighbors. This analysis found 42 UCDs with a CROWD parameter larger than 0.7 within the total sample of 71 UCDs with modulation listed in Tables 1 and 2. These tables also give the CROWD parameters, with the listed values corresponding to an average for stars observed in more than one sector. Hence, the variability amplitude of UCDs with a CROWD parameter smaller than 0.7 should be taken cautiously since these objects could be significantly affected by the flux contamination of nearby targets.

3. The Gaia DR3 UCDs with TESS Rotation Periods

Among 250 DR3 UCDs with TESS bona fide available 2 minutes cadence LCs, we have identified 71 targets presenting unambiguous periodicities, composing two subsamples. The first one is composed of 54 UCDs with high amplitude modulation, showing persistent temporal structures on timescales ranging from 0.133 to 5.81 days; the second one is composed of 17 UCDs with modulation signatures despite the low amplitude of their LCs, also with persistent temporal structures on timescales shorter than 1 day. However, an important aspect should be underlined: A closer look into the whole of the LCs of eight of these 17 UCDs with low amplitude, namely TIC 448590406, TIC 299007548, TIC 356632694, TIC 371080717, TIC 275133493, TIC 201688405, TIC 302396416, and TIC 342967337, reveals that in some epochs (TESS sectors) they show a quasi-sinusoidal modulation, while in other epochs there is a negligible or undetectable sign of variability. Tables 1 and 2 give the periods for the referred samples of 54 and 17 UCDs, respectively, including the associated error in the period (eP_{rot}), the effective time span (t_{SPAN}) of each LC (the total time span subtracted by the duration of eventual gaps), the effective number of cycles of the rotational modulation (defined as $N_{Cycle} = t_{SPAN}/P_{rot}$), and the TESS observation sectors.

We have also identified 20 DR3 UCDs with dubious or ambiguous variability signatures in their LCs. Dubious variability corresponds to targets showing a potential rotation signature but whose period could not be disentangled among two or more possibilities (from periodogram peaks and wavelet maps) and stars with $N_{Cycle} < 3$. Ambiguous variability corresponds to objects showing visually large-amplitude variations with a very irregular or complex structure in the LCs, noticeable fluctuations, or an insufficient time span to correctly

Table 3
Gaia DR3 UCDs with TESS Ambiguous or Dubious Variability

TIC ID	Gaia ID	Ambiguous or Dubious TESS Sectors	Noisy TESS Sectors	RUWE
26390890	216704503361774080	42, 43, 44	…	1.057
58108762	164474986623118592	43, 44	…	0.880
58175278	164783811951433856	43, 44	…	3.177
58229208	164702070133970944	19, 43, 44	…	1.216
58285782	164502062096975744	19, 43, 44	…	1.408
58544613	149629483705467008	43, 44	…	1.152
58601266	152029992465874560	43, 44	…	1.024
118710667	146874275068113664	43, 44	…	0.958
125882881	148449845165337600	43, 44	…	1.080
167670065	6118581861234228352	11	38	0.974
260304085	5496160698257650048	4	5, 7, 8, 10–13	0.991
346721695	216575791780899200	42, 44	43	1.004
348844681	5479241065435684352	13	5, 7, 8, 12	0.987
367089503	2279554205887675392	17, 19 ,24, 25	…	1.149
385557215	71504509626338048	42	43, 44	0.909
387813466	2270043769607851264	16, 17, 18, 24, 25	…	1.135
389053345	3311785239689504512	44	43	1.020
397367343	3480771277705948928	10	…	1.041
436574130	3406128761895775872	43, 44	…	0.964
467753980	169163647804297216	44	43	1.010

(This table is available in machine-readable form in the online article.)

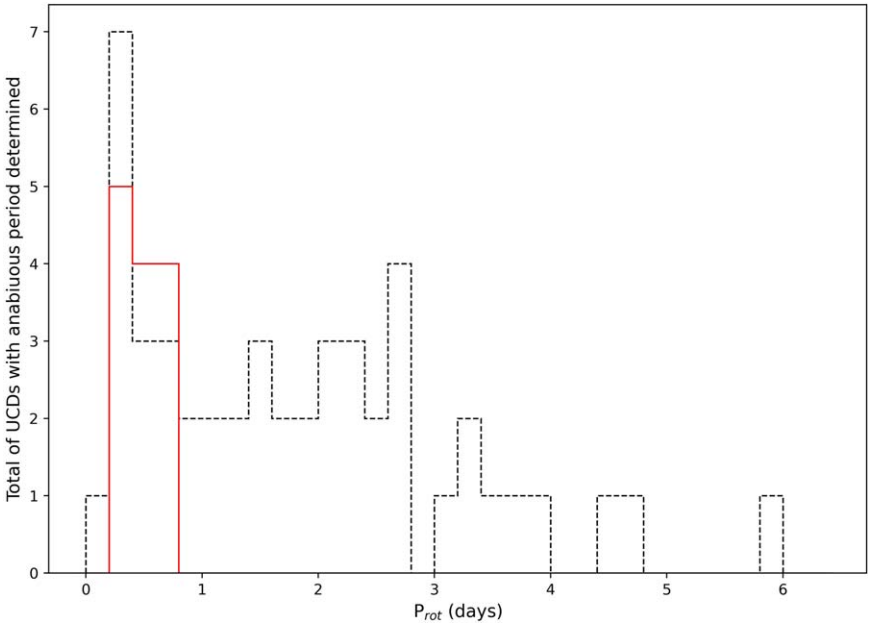

Figure 3. The distribution of rotation periods from the present analysis for the UCDs with rotation signature and single-source behavior. The dashed black histogram stands for the 48 UCDs with unambiguous rotation periods, and the red color for the 13 UCDs with unambiguous rotation and low amplitude variability in the LCs.

identify the nature of their variability signature (see Section 2.5 of Canto Martins et al. 2020). The referred UCDs are listed in Table 3 and their LCs are also provided in an online figure set given in Appendix B3. A few of these targets, TIC 125882881, TIC 367089503, TIC 58285782, and TIC 58229208, present apparent changes in their temporal structure in the same TESS sector.

Tables 1 and 2 show a relatively high number of UCDs with short-period measurements: 40% out of the 71 objects with computed periods. We carefully analyzed if some of those short periods could be associated with binarity. Then, we visually inspected the short-period LCs, searching for eclipsing binary (EB) signatures. However, no sign of binarity was found in the LCs. In this sense, we have evaluated the Gaia renormalized unit weight error (RUWE) parameter for the entire list of 71 UCDs, which may be an indicator of multiplicity (Lindegren et al. 2021). A RUWE value of around 1.0 is expected for a single-star astrometric solution. In contrast, a value significantly greater than 1.0, typically greater than 1.4, could indicate a nonsingle source or one problematic for the astrometric solution (e.g., Kervella et al. 2022). Ten targets with RUWE greater than 1.4 were identified, six from Table 1 (TIC 17518894, TIC 268325250, TIC 56002511, TIC 58229181, TIC 56624850, and TIC 902237947), and four from Table 2 (TIC 356632694, TIC 281668854, TIC 388682292, and TIC 448590406). The star TIC 58229181 is listed in the literature as an EB from TESS observations (Prša et al. 2022), whereas TIC 56624850 is classified as a circumbinary protoplanetary disk system (Czekala et al. 2019). In addition, among the UCDs with dubious or ambiguous variability signatures in their LCs, 18 present a RUWE greater than 1.4.

Then, for the present study, namely the search for rotation signatures in sources identified as UCDs in the Gaia DR3, observed by the TESS mission, we consider as potential bona fide rotation signatures only those UCDs with a RUWE less than 1.4. This criterion amounts to 48 and 13 objects from the lists given in Tables 1 and 2, respectively. The distribution of the computed rotation periods for the corresponding sample of 61 UCDs with a RUWE less than 1.4, namely those expected to be likely single-rotating objects, is displayed in Figure 3. As it arises, the periods for these UCDs range from 0.133 to 5.81 days for the sample listed in Table 1 and from 0.116 to 0.71 day for the UCDs listed in Table 2, the latter with low LC amplitudes.

Five of the UCDs listed in Table 1 have two periodicity values (TIC 150094175, TIC 20305594, TIC 359892714, TIC 58638214, and TIC 96680763), four of which present a second period at half the main period (TIC 20305594, TIC 359892714, TIC 58638214, and TIC 96680763). These cases can be interpreted as double-dip signatures (Basri & Nguyen 2018; Basri 2018), typically produced by two groups of heterogeneities on the stellar surface, such as spots, clouds, or large wave bands (e.g., Apai et al. 2017), with phases shifted by about 90°. Those phase shifts may evolve over time, producing beating effects in the LCs or a variation of the peak amplitudes in the periodograms that could be caused by differential rotation (e.g., Apai et al. 2017; Basri & Nguyen 2018; Basri 2018). In wavelet maps, a distinctive pattern often includes two dominant features over time, where one feature's period is either double or half of the other. Frequently, the longer period corresponds to the stellar rotation period, while the shorter one results from the combination of two semi-sinusoids linked to the double-dip signature (e.g., Canto Martins et al. 2020).

A no less relevant result concerns the high number of 159 targets showing noisy behavior in their LCs, corresponding to 64% of the original sample of 250 targets. Although those targets present typically low-amplitude signals whose physical periodicities cannot be easily identified, they can hide essential information. Typically, a noisy signature is a complex combination of instrumental noise contributions (related, for instance, with Poisson statistics and readout noise) plus a relevant contribution of intrinsic stellar noise, the Galactic position, light from neighboring stars, and sky background contamination (e.g., Gilliland et al. 2011). When the LCs considered in this work present a low-amplitude signal, we assumed them to be, in principle, a noisy signature. The noisy

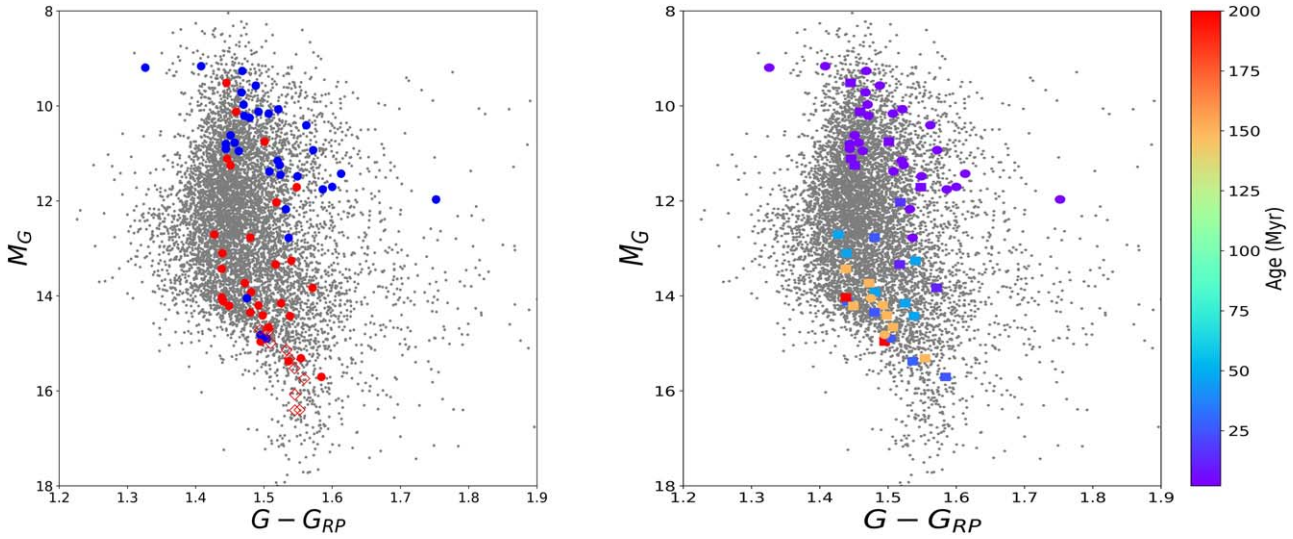

Figure 4. The Gaia CMD for the sample of UCDs comprising the present study, with black circles illustrating the whole sample of 7630 Gaia DR3 UCDs, given by Sarro et al. (2023). In the left panel circles in blue are for the UCDs with $P_{\rm rot} \geqslant 1.0$ day, red circles are for the UCDs with $P_{\rm rot} < 1$ day, and red open diamonds stand for the UCDs listed by Miles-Páez et al. (2023). In the right panel, colors follow the color bar age intervals, which gives the age in millions of years.

behavior could reflect low activity or long periods for some stars, particularly for targets with short observational time spans. Table A2 in the Appendix gives the list of UCDs supposedly presenting noisy LCs.

Miles-Páez et al. (2023) have analyzed the TESS LCs of a sample of 23 known rapidly rotating UCDs, typically objects with a $V \sin i > 30$ km s^{-1} to explore their photometric variability. The authors used a Lomb–Scargle periodogram in their study, applying a first-order correction by removing a 24 hr median filter from the data and then a Gaussian-process regression. From such an analysis, they claimed that significant periodicities in 18 targets are compatible with a rotation signature, with amplitudes ranging from 0.17% to 0.77%. For comparative purposes, even though only two UCDs from Miles-Páez et al. (2023) are present in our whole list of Gaia DR3 UCDs, we have then applied our manifold procedure to the 21 targets of their sample with 2 minutes cadence LCs available. The result of this analysis is presented in Table 4, from where one can observe that, for most cases, our variability periods are in good agreement with those computed by Miles-Páez et al. (2023), except for three targets (TIC 288506050, TIC 441000085, and TIC 311188315), for which our analysis points instead to a noisy behavior in their LCs. Further, it is worth underlining that among the 21 UCDs listed in Table 4, 10 have a RUWE greater than 1.4. Recently, Petrucci et al. (2024) have reported rotation periods for a sample of 87 UCDs from TESS LCs, based on a Lomb–Scargle periodogram. Among these objects, 80% show $P_{\rm rot} < 1$ day. Four objects from the referred sample (TIC 298907057, TIC 902237947, TIC 201688405, and TIC 371080717) are in common with our study, showing a good agreement in the corresponding $P_{\rm rot}$ values.

The locations of the Gaia DR3 UCDs with rotation periods and RUWE shorter than 1.4, listed in Tables 1, 2, and 4, are shown in the color–magnitude diagram (CMD) displayed in Figure 4, from where one can observe an apparent trend for a transition in the distribution of UCD rotation periods. In the left panel, UCDs with $P_{\rm rot} \geqslant 1.0$ day tend to be located mainly in the regions above $11.5 < M_G < 12.5$, whereas those with $P_{\rm rot} < 1.0$ day tend to populate the region below this range. In addition, the CMD diagram in the aforementioned panel also appears to point to a dependence on the distribution of $P_{\rm rot}$ with stellar mass, separated into two different regimes. The upper region, populated mainly by UCDs with $P_{\rm rot} \geqslant 1.0$ day, is composed of lower-mass M stars, whereas the lower region, mainly populated by UCDs with $P_{\rm rot} < 1.0$ day, is composed of larger-mass M stars (Reylé 2018). Thanks to the nature of the present UCD sample, which consists of objects located in stellar associations with measured ages (Kenyon & Hartmann 1995; Zuckerman et al. 2006, 2011; Murphy et al. 2013; Bell et al. 2015; Pecaut & Mamajek 2016), the right panel in Figure 4 displays the same CMD. In this panel, stars are separated into age intervals based on the values given in Tables 1 and 2, to tentatively define regions where younger and older stars are expected to dominate. The scenario emerging from the right panel in Figure 4 indicates an interesting trend: UCDs with $P_{\rm rot} \geqslant 1.0$ day tend to be located mainly in the regions of younger objects, whereas those with $P_{\rm rot} < 1.0$ day tend to populate the regions occupied by older objects.

Nevertheless, we should be cautious with the referred trend observed in the CMD diagram, which could be affected by observational biases. The incompleteness of the analyzed UCD sample and the instrumental sensitivity in the observed wavelength band may contribute to the portrait observed in the rotation period distribution (e.g., Leão et al. 2015; Canto Martins et al. 2023). For instance, the UCD sample may be incomplete to periods longer than 24 hr because TESS is mainly sensitive to L0 dwarfs and, on the other side, the lower period limits are also uncertain because most UCD campaigns have been limited to ∼8–24 hr cadences (Miles-Páez et al. 2023). Besides, the region with an apparent lack of stars with rotation period measurements could be populated by low-amplitude rotators below the TESS sensitivity. Despite these potential biases, it is worth underlining that, based on the analysis of the projected rotation velocity $V \sin i$ of UCDs, Mohanty & Basri (2003) showed that this parameter tends to increase from mid-M to L types and that L-type UCDs are probably rapidly rotating in general, with a lack of slowly rotating stars in this latter spectral region.

Table 4
Gaia DR3 UCDs with Previous TESS Periodicities in the Literature

TIC ID	P_{rot} (hr)	Amplitude (%)	TESS Sectors With Modulation – This Work	TESS Sectors Noisy – This Work	P_{rot} (hr)	Amplitude (%)	TESS Sectors	CROWD	RUWE
	This Work				Miles-Páez et al. (2022)				
8259901	3.072 ± 0.007	0.93	21	…	2.5267 ± 0.0002	0.44 ± 0.01	21	0.240	2.785
8259902	3.072 ± 0.005	0.26	21, 48	…	3.0889 ± 0.0002	0.44 ± 0.01	21	0.829	1.498
16227031	…	…	…	44, 45, 46	…	…	44	0.663	1.212
17308656	…	…	…	…	4.9199 ± 0.0035	0.58 ± 0.08	43, 44	…	2.794
27858644	2.832 ± 0.002	0.17	26, 40, 54	53	2.84140 ± 0.00039	0.34 ± 0.03	26, 40	0.703	1.096
32422219	2.112 ± 0.002	0.19	3, 30	…	2.15012 ± 0.00024	0.53 ± 0.06	3,30	0.902	2.698
34014829	3.859 ± 0.007	0.24	2, 29	…	3.8632 ± 0.0016	0.44 ± 0.03	2, 29	0.892	5.417
143029977	3.840 ± 0.014	0.1	31	4	3.8356 ± 0.0010	0.17 ± 0.04	4, 31	0.888	0.999
193974787	3.072 ± 0.009	0.24	16	23, 24, 49, 51	3.0942 ± 0.0010	0.48 ± 0.08	16, 23, 24	0.651	0.998
198107795	11.292 ± 0.039	0.52	16, 23, 49, 50	…	11.4334 ± 0.0058	0.59 ± 0.03	16, 23	0.845	11.011
202408306	15.336 ± 0.153	0.76	23, 50	…	15.34 ± 0.03	0.66 ± 0.06	23	0.993	0.946
219095664	3.888 ± 0.001	0.24	14–21, 24 25, 55, 57, 58	22, 23, 40, 41 47–52, 54, 56, 59	3.89442 ± 0.00041	0.18 ± 0.04	14–25, 40, 41	0.852	4.316
229653723	…	…	…	…	…	<0.34	22	…	1.231
239097694	…	…	…	19, 59	…	…	19	0.267	0.993
286963145	…	…	…	23	…	<0.28	23	0.962	1.095
288506050	…	…	…	16, 22, 23	2.4221 ± 0.0003	0.70 ± 0.05	16, 22, 23	0.986	1.178
307956653	3.614 ± 0.001	0.4	16–19, 21, 22, 25, 26, 40 41, 47–50, 53, 55–58, 60	14, 15, 24, 51 52, 54, 59	3.62703 ± 0.00031	0.49 ± 0.1	14–26, 40, 41	0.853	1.150
311188315	…	…	…	24, 51	1.95976 ± 0.00043	0.43 ± 0.08	24	0.372	1.661
438883548	…	…	…	…	3.992 ± 0.017	0.42 ± 0.07	11	…	1.445
441000085	…	…	…	11, 38	3.9614 ± 0.0009	0.77 ± 0.06	11, 38	0.831	1.185
902237947	6.000 ± 0.036	3.93	36	…	5.984 ± 0.001	0.6 ± 0.02	9	0.210	3.117

(This table is available in machine-readable form in the online article.)

4. Summary and Conclusions

Based on a manifold procedure, which considers the analysis of TESS LCs taking into account Lomb–Scargle periodograms, FFTs, and wavelet transforms, we have analyzed a total of 250 Gaia DR3 UCDs presenting public LCs, with short-cadence TESS observations in Sectors 5–63. We identified 48 UCDs with rotational modulation, presenting an unambiguous rotation period. Among these UCDs, five show two periods, with four presenting a second period that is approximately double or half of the rotation period. This aspect may reveal the presence of differential rotation in the referred targets. We have also identified 13 UCDs with typical modulation signatures, presenting periods shorter than 1 day despite a low-amplitude behavior in their LCs. Ten UCDs with unambiguous periodicities show a potential nonsingle behavior, pointing to a dubious origin of the referred periodicities. The present study also revealed 20 UCDs with ambiguous or dubious variability signatures in their LCs, a few of them with LCs presenting apparent changes in the temporal structure. The TESS LCs for the remaining 159 objects show a noisy pattern with very-low-amplitude signals.

Considering the whole sample of UCDs with rotation periods, this study shows that 47.5% have a period shorter than 1 day. Another relevant result arises from the CMD diagram, which seems to show a lack of rotating UCDs within about $11.5 < M_G < 12.5$ and $G–G_{RP} < 1.5$ that separates them into two different regimes. One is mainly composed of less massive late-M stars with $P_{rot} \geqslant 1.0$ day, and the other regime is mainly composed of more massive early-M stars with $P_{rot} < 1.0$ day. Also, by separating the stars into age intervals, we found that UCDs with $P_{rot} \geqslant 1.0$ day tend to be in regions of younger objects, while those with $P_{rot} < 1.0$ day are concentrated in regions of older objects. Whether the apparent lack of stars contrasting the sample separation is physical or produced by observational biases is a question to be verified in future studies based on a more extensive and homogeneous sample, as well as better statistics. If, on one side, the signatures of rotation in UCDs are associated with multiple origins, including magnetic processes, condensate particles that form atmospheric cloud-like structures, or even brightness changes due to an atmosphere out of chemical equilibrium, the objects with ambiguous variability or a noisy pattern appear to reflect also the presence of different factors, such as low-activity phases or polar phenomena. In this context, the large collection of bona fide rapidly rotating UCDs revealed in the present work represents a solid sample with which to identify the cause of photometric variability in UCDs through spectroscopic analysis, in particular to identify traces that can differentiate between magnetically induced starspots and inhomogeneous atmospheric dust clouds. A first step in this direction should be the study of their spectroscopic line profiles. If these targets are rapidly rotating, their line profiles will be significantly Doppler broadened. The large sample of noisy UCDs also offers relevant material for spectroscopic studies. If such behavior reflects a low activity level and a slow rotation, these objects will not show much line broadening. Identifying the root cause of photometric variability in UCDs is also mandatory to understand the structural stability of rapidly rotating UCDs.

Acknowledgments

Research activities of the Observational Astronomy Board at the Federal University of Rio Grande do Norte (NAOS) are supported by continuous grants from the Brazilian funding agency CNPq. This study was financed in part by the Coordenação de Aperfeiçoamento de Pessoal de Nível Superior – Brasil (CAPES) – Finance Code 001. Y.S.M. and D.O.F. acknowledge CAPES graduate fellowships, and R.L.G. acknowledges a CNPq PDE fellowship. P.D.S.L. and Y.S.M. acknowledge a UFRN/CAPES/Print fellowship, respectively, process 88887.838338/2023-00 and 88887.717782/2022-00. J.M.A. acknowledges the CNPq Brazilian research agency for funding (grant No. 311589/2021-9). B.L.C.M. (grant No. 305804/2022-7), I.C.L. (grant No. 313103/2022-4), and J.R.M. (grant No. 308928/2019-9) acknowledge CNPq research fellowships. This work includes data collected by the TESS mission. The NASA Explorer Program provides funding for the TESS mission. All the TESS data used in this paper can be found in MAST (10.17909/fwdt-2x66). We made use of data from the European Space Agency (ESA) mission Gaia (http://www.cosmos.esa.int/gaia), processed by the Gaia Data Processing and Analysis Consortium (DPAC; https://www.cosmos.esa.int/web/gaia/dpac/consortium). Funding for the DPAC has been provided by national institutions, particularly the institutions participating in the Gaia Multilateral Agreement. We want to thank the referee for carefully reading the manuscript and a number of suggestions that largely improved the paper.

Appendix A
Machine-readable Materials

Tables A1 and A2 present the lists of Gaia DR3 UCDs. Table A1 contains 250 UCDs with bona fide TESS LCs, while Table A2 lists 159 UCDs supposedly presenting noisy TESS LCs.

Table A1
List of 250 Gaia DR3 UCDs with Available TESS LCs

TIC ID	Gaia ID	SpT	M_G (mag)	G (mag)	$G_{BP} - G_{RP}$ (mag)	$G_{BP} - G$ (mag)	G–G_{RP} (mag)	Association Clustering
1274822	4873243032763432064	M9	16.736	18.4263	4.677	3.087	1.59	ARG
5630425	3493736924979792768	M7	14.898	15.0966	4.806	3.303	1.504	BPMG
7652166	4841023012742841216	M9	14.141	18.6194	3.653	2.062	1.591	COL
8940069	2438826436627893248	M7	13.909	16.3539	4.439	2.938	1.501	CARN
11311177	5658599213249509120	M9	17.201	20.6952	2.402	0.773	1.63	CARN
11713886	1828402423000351616	M7	14.220	16.5640	4.602	3.122	1.48	ABDMG
14252664	65937712317870592	M7	12.853	18.5839	4.051	2.585	1.467	PLE
14284933	53049516189920384	M5	13.476	19.0613	3.430	2.005	1.425	PLE

(This table is available in its entirety in machine-readable form in the online article.)

Table A2
List of 159 Gaia DR3 UCDs with TESS Noisy LCs

TIC ID	Gaia ID	TESS Sectors
1274822	4873243032763432064	5
7652166	4841023012742841216	4, 5
8940069	2438826436627893248	42
11311177	5658599213249509120	8, 9
11713886	1828402423000351616	14, 54
14252664	65937712317870592	43, 44
14284933	53049516189920384	44

(This table is available in its entirety in machine-readable form in the online article.)

Appendix B
Online Figures

Figures B1, B2, and B3 display the diagnostic plots for Gaia DR3 UCDs. Figure B1 shows FFT and Lomb–Scargle periodograms, LCs, phase-folded LCs, and wavelet maps for the stellar sample with typical TESS rotation signatures. Figure B2 presents similar plots for the sample with typical TESS rotation signatures and low amplitude. Figure B3 displays the LCs for those with ambiguous or dubious TESS variability.

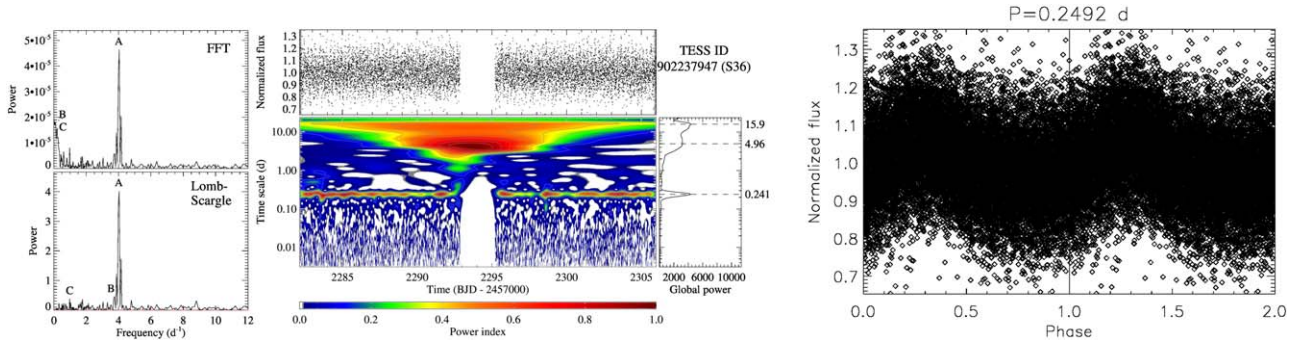

Figure B1. The diagnostic plots displaying FFT and Lomb–Scargle periodograms, LCs, phase-folded LCs, and wavelet maps for the entire sample of Gaia DR3 UCDs with typical TESS rotation signatures, listed in Table 1. The complete figure set (120 images, one image per object and TESS sector) is available in the online journal.
(The complete figure set (120 images) is available in the online article.)

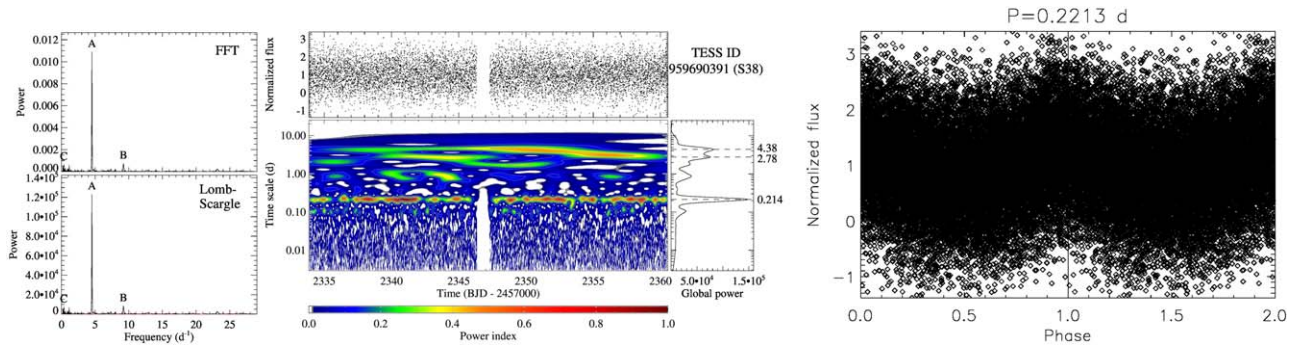

Figure B2. The diagnostic plots displaying FFT and Lomb–Scargle periodograms, LCs, phase-folded LCs, and wavelet maps for the sample of Gaia DR3 UCDs with typical TESS rotation signatures and low amplitude, listed in Table 2. The complete figure set (50 images, one image per object and TESS sector) is available in the online journal.

(The complete figure set (50 images) is available in the online article.)

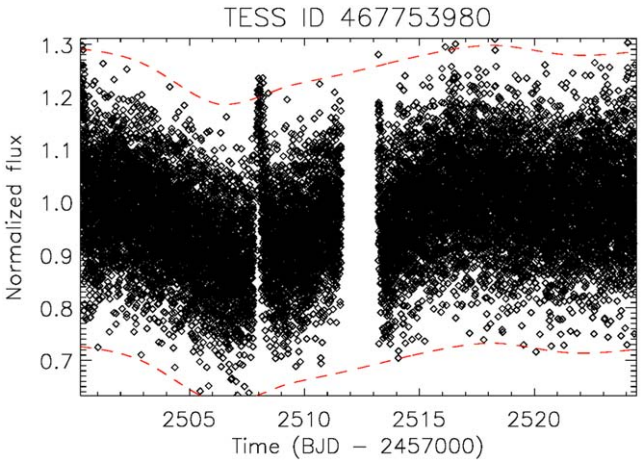

Figure B3. The LCs for the Gaia DR3 UCDs with TESS ambiguous or dubious variability, listed in Table 3. The complete figure set (57 images, one image per object and TESS sector) is available in the online journal.

(The complete figure set (57 images) is available in the online article.)

ORCID iDs

P. D. S. de Lima https://orcid.org/0000-0002-7353-536X
Y. S. Messias https://orcid.org/0000-0002-2425-801X
C. E. Ferreira Lopes https://orcid.org/0000-0002-8525-7977
B. L. Canto Martins https://orcid.org/0000-0001-5578-7400
I. C. Leão https://orcid.org/0000-0001-5845-947X
J. M. De Araújo https://orcid.org/0000-0001-8462-4280
E. Janot Pacheco https://orcid.org/0000-0003-0079-3912
J. R. De Medeiros https://orcid.org/0000-0001-8218-1586

References

Apai, D., Karalidi, T., Marley, M. S., et al. 2017, Sci, 357, 683
Artigau, É., Bouchard, S., Doyon, R., et al. 2009, ApJ, 701, 1534
Bailer-Jones, C. A. L. 2004, A&A, 419, 703
Barclay, T., Pepper, J., & Quintana, E. V. 2018, ApJS, 239, 2
Barraza, L. F., Gomes, R. L., Messias, Y. S., et al. 2022, ApJ, 924, 117
Basri, G. 2018, ApJ, 865, 142
Basri, G., & Nguyen, H. T. 2018, ApJ, 863, 190
Bell, C. P. M., Mamajek, E. E., & Naylor, T. 2015, MNRAS, 454, 593
Buenzli, E., Apai, D., Radigan, J., et al. 2014, ApJ, 782, 77
Burgasser, A. J., Kirkpatrick, J. D., Brown, M. E., et al. 2002, ApJ, 564, 421
Burningham, B., Pinfield, D. J., Leggett, S. K., et al. 2008, MNRAS, 391, 320
Caldwell, D. A., Tenenbaum, P., Twicken, J. D., et al. 2020, RNAAS, 4, 201
Canto Martins, B. L., Gomes, R. L., Messias, Y. S., et al. 2020, ApJS, 250, 20
Canto Martins, B. L., Messias, Y. S., Arruda Gonçalves, M. I., et al. 2023, NatAs, 7, 900
Cushing, M. C., Hardegree-Ullman, K. K., Trucks, J. L., et al. 2016, ApJ, 823, 152
Czekala, I., Chiang, E., Andrews, S. M., et al. 2019, ApJ, 883, 22
De Medeiros, J. R., Ferreira Lopes, C. E., Leão, I. C., et al. 2013, A&A, 555, A63
Donati, J.-F., Lehmann, L. T., Cristofari, P. I., et al. 2023, MNRAS, 525, 2015
Doyle, L., Ramsay, G., & Doyle, J. G. 2020, MNRAS, 494, 3596
Ferreira Lopes, C. E., Leão, I. C., de Freitas, D. B., et al. 2015, A&A, 583, A134
Gagné, J., Mamajek, E. E., Malo, L., et al. 2018, ApJ, 856, 23
Gilliland, R. L., Chaplin, W. J., Dunham, E. W., et al. 2011, ApJS, 197, 6
Grossmann, A., & Morlet, J. 1984, SIAM Journal on Mathematical Analysis, 15, 723
Harding, L. K., Hallinan, G., Boyle, R. P., et al. 2013, ApJ, 779, 101
Higgins, M. E., & Bell, K. J. 2023, AJ, 165, 141
Hooten, J. T., & Hall, D. S. 1990, ApJS, 74, 225
Horne, J. H., & Baliunas, S. L. 1986, ApJ, 302, 757
Irwin, J., Berta, Z. K., Burke, C. J., et al. 2011, ApJ, 727, 56
Jenkins, J. M., Twicken, J. D., McCauliff, S., et al. 2016, Proc. SPIE, 9913, 99133E
Kenyon, S. J., & Hartmann, L. 1995, ApJS, 101, 117
Kervella, P., Arenou, F., & Thévenin, F. 2022, A&A, 657, A7
Kirkpatrick, J. D., Reid, I. N., Liebert, J., et al. 1999, ApJ, 519, 802
Koen, C., Tanabé, T., Tamura, M., et al. 2005, MNRAS, 362, 727
Lamm, M. H., Bailer-Jones, C. A. L., Mundt, R., et al. 2004, A&A, 417, 557
Leão, I. C., Pasquini, L., Ferreira Lopes, C. E., et al. 2015, A&A, 582, A85
Lindegren, L., Klioner, S. A., Hernández, J., et al. 2021, A&A, 649, A2
Metchev, S. A., Heinze, A., Apai, D., et al. 2015, ApJ, 799, 154
Miles-Páez, P. A., Metchev, S. A., & George, B. 2023, MNRAS, 521, 952
Miles-Páez, P. A., Pallé, E., & Zapatero Osorio, M. R. 2017, MNRAS, 472, 2297
Mohanty, S., & Basri, G. 2003, ApJ, 583, 451
Mullally, S. E., Sloan, G. C., Hermes, J. J., et al. 2022, AJ, 163, 136
Murphy, S. J., Lawson, W. A., & Bessell, M. S. 2013, MNRAS, 435, 1325
Paz-Chinchón, F., Leão, I. C., Bravo, J. P., et al. 2015, ApJ, 803, 69
Pecaut, M. J., & Mamajek, E. E. 2013, ApJS, 208, 9
Pecaut, M. J., & Mamajek, E. E. 2016, MNRAS, 461, 794
Pedersen, M. G., & Bell, K. J. 2023, AJ, 165, 239
Petrucci, R. P., Gómez Maqueo Chew, Y., Jofré, E., et al. 2024, MNRAS, 527, 8290
Pineda, J. S., Hallinan, G., & Kao, M. M. 2017, ApJ, 846, 75
Press, W. H., & Rybicki, G. B. 1989, ApJ, 338, 277
Prša, A., Kochoska, A., Conroy, K. E., et al. 2022, ApJS, 258, 16
Radigan, J., Lafrenière, D., Jayawardhana, R., et al. 2014, ApJ, 793, 75
Reylé, C. 2018, A&A, 619, L8
Ricker, G. R., Winn, J. N., Vanderspek, R., et al. 2015, JATIS, 1, 014003
Rockenfeller, B., Bailer-Jones, C. A. L., & Mundt, R. 2006, A&A, 448, 1111
Sarro, L. M., Berihuete, A., Smart, R. L., et al. 2023, A&A, 669, A139
Saumon, D., Geballe, T. R., Leggett, S. K., et al. 2000, ApJ, 541, 374
Scargle, J. D. 1982, ApJ, 263, 835
Suárez, G., & Metchev, S. 2023, MNRAS, 523, 4739

Tannock, M. E., Metchev, S., Heinze, A., et al. 2021, AJ, 161, 224
Tinney, C. G., & Tolley, A. J. 1999, MNRAS, 304, 119
Tremblin, P., Amundsen, D. S., Mourier, P., et al. 2015, ApJL, 804, L17
Tsuji, T., Ohnaka, K., Aoki, W., et al. 1996, A&A, 308, L29
Vos, J. M., Faherty, J. K., Gagné, J., et al. 2022, ApJ, 924, 68
Wang, Y. 2021, Geop, 86, V31
Wang, Y. 2022, Geophysics, Time-Frequency Analysis of Seismic Signals (New York: Wiley)
Zahnle, K. J., & Marley, M. S. 2014, ApJ, 797, 41
Zhan, Z., Günther, M. N., Rappaport, S., et al. 2019, ApJ, 876, 127
Zuckerman, B., Bessell, M. S., Song, I., et al. 2006, ApJL, 649, L115
Zuckerman, B., Rhee, J. H., Song, I., et al. 2011, ApJ, 732, 61